I. Troch, F. Breitenecker, eds. ISBN 978-3-901608-35-3

FASTER LOAD CHANGES FOR MOLTEN CARBONATE FUEL CELL SYSTEMS

K. Chudej[1], K. Sternberg[2], H.J. Pesch[1]
[1]Universität Bayreuth, Germany, [2]Merz Pharmaceuticals GmbH, Frankfurt, Germany

Corresponding author: K. Chudej, Universität Bayreuth, Lehrstuhl für Ingenieurmathematik, 95440 Bayreuth, Germany, kurt.chudej@uni-bayreuth.de

Abstract. Molten carbonate fuel cells are a promising technology for operating future stationary power plants. In order to enhance service life, a detailed understanding of the dynamical behavior of such fuel cell systems is needed. In particular, high temperature gradients of the solid temperature have to be strictly avoided. On the other hand, it is desirable to perform load changes as fast as possible. For that purpose, a family of hierarchically ordered mathematical models has been developed with the aim to simulate and optimize the dynamical behavior with respect to fast load changes without risking material corrosion due to extreme thermal fluctuations. This leads to a Pareto-type optimal control problem with constraints in form of a system of equations that are staggered with respect to their time scales and are composed of degenerated partial differential equations as well as integro differential-algebraic equations.

In this article, we present optimal control results which address both, sufficiently fast load changes and sufficiently small fluctuations of the solid temperature, by employing the different time scales of the variables.

1 Introduction

Molten carbonate fuel cell systems (MCFC) are an efficient and environmentally friendly technology for the simultaneous stationary production of electrical energy and heat (resp. cooling) [17, 19].

MCFC belong to the class of high temperature fuel cells. The operation temperature is about 600°C. In contrast to low temperature fuel cells, the temperature is high enough to allow for internal reforming, i.e. to produce hydrogen internally in the cell system from different kinds of fuel gases (e.g. CH_4). Moreover, neither expensive catalysts nor expensive ceramics are needed for an efficient operation. Due to the high operating temperatures, it is difficult to operate MCFCs. One has to stay within a certain range of admissible temperatures. Chemical and electrochemical reactions decelerate in regions of low temperature, whereas in regions of high temperature fast catalyst degradation appears. Temperature gradients have to be moderate in order to avoid material corrosion due to temperature induced stresses. Therefore the cell temperatures are crucial for the system's performance and lifetime.

MCFC systems are being developed and tested by several companies around the world and can be expected to become competitive to classical power plants within the next few years [1, 10, 11, 13]. Nevertheless, efforts are necessary to increase their efficiency, to develop better control strategies, and to improve long time stability. Besides experimental validations, mathematical models are an indispensable tool to achieve these goals. Potentially dangerous or even disastrous control scenarios for real stacks of fuel cells can be safely simulated by means of mathematical models. Realistic mathematical models [6, 9] based on *physical* and *chemical laws* have paved the road to apply mathematical optimization and optimal control techniques [14]. Moreover mathematical models allow to study the consequences of modified designs in advance such as crossflow versus counterflow designs [14] or different (optimal) catalyst distribution [7].

A general description of different fuel cell types can be found in the book of Winkler [19]. Recent results on molten carbonate fuel cells are collected in the book [17]. The mathematical model used therein is part of a hierarchically ordered family of models; for details see the thesis of Heidebrecht [6] and [9]. This article is based on the thesis [14] and presents, for the first time, optimal control results, which take into account more strictly the two contradicting engineering objectives: faster load changes *and* smaller fluctuations of the solid temperature.

2 The 2D Molten Carbonate Fuel Cell Model

The mathematical model of Heidebrecht [6], see also [9, 14], which is investigated in the present paper, describes an averaged single MCFC of the stack of about 350 cells. The model is based on physical and chemical laws for the gas transport and the electro-chemical reactions which take place in each single fuel cell. The underlying design is a crossflow configuration with respect to the anode and cathode gas flows; see Fig. 1. This figure shows a 3D view of the compartments of the anode and cathode gas channels, the solid/electrolyte, the catalytic burner and mixer, and the configuration of the gas flows. In the anode/cathode compartments, the fuel gas actually flows through several small pipes parallel to the ζ_1-axis/ζ_2-axes. In fact, the cell is very flat. Therefore, the third dimension ζ_3 can be neglected. Such a design has been realized for the so-called *HotModule* produced by the MTU CFC Solutions GmbH (Munich) [10], and is operated among others by the IPF-Heizkraftwerksbetriebsgesellschaft

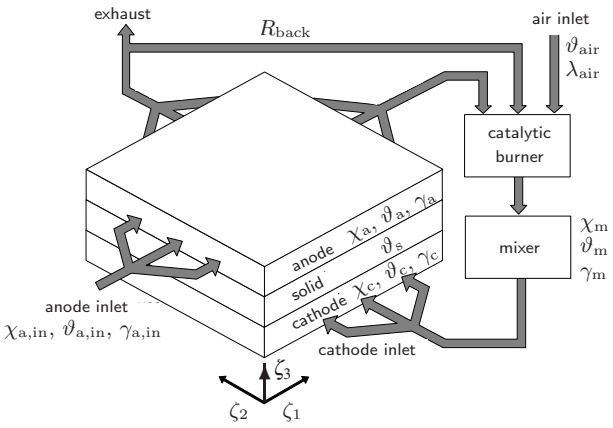

Figure 1: Cross flow model of a MCFC with compartments and mathematical variables

mbH, Magdeburg at the power plant of the University Hospital of Magdeburg [11]. A closely related mathematical model was validated for the above mentioned power plant [5].

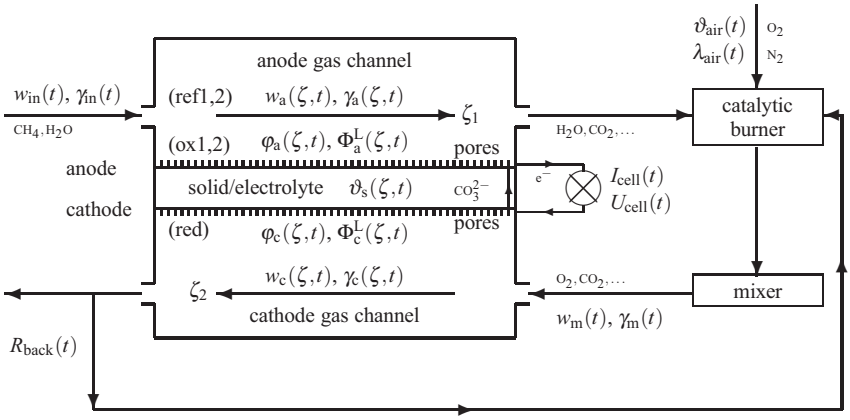

(ref1) $CH_4 + H_2O \rightleftharpoons CO + 3H_2$ (ref2) $CO + H_2O \rightleftharpoons CO_2 + H_2$

(ox1) $H_2 + CO_3^{2-} \rightleftharpoons H_2O + CO_2 + 2e^-$ (ox2) $CO + CO_3^{2-} \rightleftharpoons 2CO_2 + 2e^-$

(red) $\frac{1}{2}O_2 + CO_2 + 2e^- \rightleftharpoons CO_3^{2-}$

Figure 2: 2D crossflow model of a molten carbonate fuel cell with variables $w = (\chi, \vartheta)$, χ =vector of molar fractions, ϑ =temperature, φ =vector of partial pressures, Φ =electrical potentials, U_{cell} =cell voltage, I_{cell} =cell current

The more detailed Fig. 2 additionally depicts the variables in the pores and the considered chemical reactions: the reforming reactions (ref 1,2) take place in the anode gas channel, the oxidation reactions (ox 1,2) in the pores of the anode, the reduction reaction in the pores of the cathode. The compartments are denoted by an index k: a = anode gas channel/anode pores, c = cathode gas channel/cathode pores, s = solid, e = electrolyte, m = mixer, in = inlet, out = outlet. The seven gas components are denoted by the index set $\mathscr{I} := \{CH_4, H_2O, H_2, CO, CO_2, O_2, N_2\}$ for the molar fractions $\chi_{k,j}$ and partial pressures $\varphi_{k,j}$, $j \in \mathscr{I}$, $k \in \{\text{a}, \text{c}, \text{m}\}$. Furthermore, we have to take into account the molar flow densities γ_k as well as the gas temperatures ϑ_k, $k \in \{\text{a}, \text{c}, \text{m}\}$. The gas temperatures ϑ_{a} and ϑ_{c}, see (2, 3), are dominated by convection and have to be distinguished from the solid temperature ϑ_{s}, which is distributed through the solid by heat conduction, see (1). $1 - R_{\text{back}}(t)$ denotes the fraction of the gas stream from the anode outlet which goes to the exhaust.

The electric potential, which is spatially distributed in the MCFC, is essential for the dynamical behavior. This model part is based on the spatially 1D version of Poisson's law and discrete charge layers. We assume spatially constant electric potentials at the electrodes, transport of the carbonate ions orthogonal to the $\zeta_1\zeta_2$-cell plane and transient charge balances. Moreover, the electrical potentials $\Phi_{\text{a}}^{\text{L}}$, $\Phi_{\text{c}}^{\text{L}}$, and U_{cell}, at which the anode ion layer, the cathode ion layer and the cathode electrode are relative to a reference potential $\Phi_{\text{a}}^{\text{s}} = 0$, and the current densities i_k as well as the currents I_k, $k \in \{\text{a}, \text{c}, \text{e}\}$, in the electrolyte are also incorporated in the model (see Fig. 3 and (7–11)).

The total cell current $I_{\text{cell}}(t)$ usually is prescribed either by a constant or a piecewise constant step function. Finally, the following notations are introduced: $w_k = (\chi_k, \vartheta_k)$, $w_{a|c} = (w_{\text{a}}, w_{\text{c}})$, $\Phi_{\text{a|c}}^{\text{L}} = (\Phi_{\text{a}}^{\text{L}}, \Phi_{\text{c}}^{\text{L}})$.

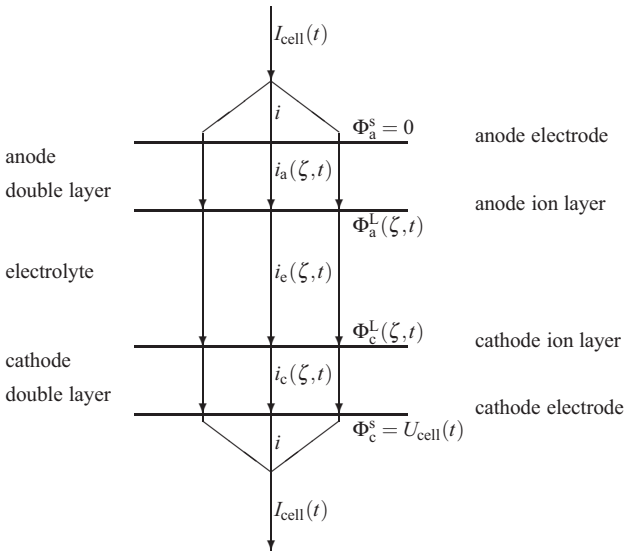

Figure 3: Electric potential field model

Altogether, we end up with a system of time dependent nonlinear partial differential algebraic equations in two spatial coordinates $\zeta := (\zeta_1, \zeta_2) \in \Omega := [0,1] \times [0,1]$. The boundary of Ω is denoted by $\partial\Omega$.

All variables are dimensionless, one unit of the dimensionless time t equals 12.5 seconds.

2.1 Mathematical Model Equations

The ingredients of the model are:

1. A system of partial differential-algebraic equations with boundary conditions:

$$\frac{\partial \vartheta_{\text{s}}}{\partial t} = \kappa_1 \frac{\partial^2 \vartheta_{\text{s}}}{\partial \zeta_1^2} + \kappa_2 \frac{\partial^2 \vartheta_{\text{s}}}{\partial \zeta_2^2} + \psi_1(\vartheta_{\text{s}}, w_{\text{a|c}}, \varphi_{\text{a|c}}, \Phi_{\text{a|c}}^{\text{L}}, U_{\text{cell}}), \quad \frac{\partial \vartheta_{\text{s}}}{\partial n}|_{\partial\Omega} = 0, \tag{1}$$

$$\frac{\partial w_{\text{a}}}{\partial t} = -\gamma_{\text{a}} \vartheta_{\text{a}} \frac{\partial w_{\text{a}}}{\partial \zeta_1} + \psi_2(\vartheta_{\text{s}}, w_{\text{a}}, \varphi_{\text{a}}, \Phi_{\text{a}}^{\text{L}}), \quad w_{\text{a}}|_{\partial\Omega_{\text{a,in}}} = w_{\text{in}}(t), \tag{2}$$

$$\frac{\partial w_{\text{c}}}{\partial t} = -\gamma_{\text{c}} \vartheta_{\text{c}} \frac{\partial w_{\text{c}}}{\partial \zeta_2} + \psi_3(\vartheta_{\text{s}}, w_{\text{c}}, \varphi_{\text{c}}, \Phi_{\text{c}}^{\text{L}}, U_{\text{cell}}), \quad w_{\text{c}}|_{\partial\Omega_{\text{c,in}}} = w_{\text{m}}(t), \tag{3}$$

$$0 = -\frac{\partial(\gamma_{\text{a}} \vartheta_{\text{a}})}{\partial \zeta_1} + \psi_4(\vartheta_{\text{s}}, w_{\text{a}}, \varphi_{\text{a}}, \Phi_{\text{a}}^{\text{L}}), \quad \gamma_{\text{a}}|_{\partial\Omega_{\text{a,in}}} = \gamma_{\text{in}}(t), \tag{4}$$

$$0 = -\frac{\partial(\gamma_{\text{c}} \vartheta_{\text{c}})}{\partial \zeta_2} + \psi_5(\vartheta_{\text{s}}, w_{\text{c}}, \varphi_{\text{c}}, \Phi_{\text{c}}^{\text{L}}, U_{\text{cell}}), \quad \gamma_{\text{c}}|_{\partial\Omega_{\text{c,in}}} = \gamma_{\text{m}}(t), \tag{5}$$

$$0 = \psi_6(\vartheta_{\text{s}}, \chi_{\text{a}}, \varphi_{\text{a}}, \Phi_{\text{a}}^{\text{L}}), \qquad 0 = \psi_7(\vartheta_{\text{s}}, \chi_{\text{c}}, \varphi_{\text{c}}, \Phi_{\text{c}}^{\text{L}}, U_{\text{cell}}), \tag{6}$$

$$\frac{\partial \Phi_{\text{a}}^{\text{L}}}{\partial t} = (i_{\text{a}} - i)/c_{\text{a}}, \qquad \frac{\partial \Phi_{\text{c}}^{\text{L}}}{\partial t} = (i_{\text{a}} - i)/c_{\text{a}} + (i_{\text{e}} - i)/c_{\text{e}}. \tag{7}$$

Only six partial pressures in (6) have to be computed numerically. This yields 25 equations.

2. A system of integro differential-algebraic equations:

$$\frac{dU_{\text{cell}}}{dt} = \frac{I_{\text{a}} - I_{\text{cell}}}{c_{\text{a}}} + \frac{I_{\text{e}} - I_{\text{cell}}}{c_{\text{e}}} + \frac{I_{\text{c}} - I_{\text{cell}}}{c_{\text{c}}}, \tag{8}$$

$$I_{\text{a}}(t) = \int_{\Omega} i_{\text{a}}(\vartheta_{\text{s}}, w_{\text{a}}, \varphi_{\text{a}}, \Phi_{\text{a}}^{\text{L}})\, d\zeta, \tag{9}$$

$$I_{\text{c}}(t) = \int_{\Omega} i_{\text{c}}(\vartheta_{\text{s}}, w_{\text{c}}, \varphi_{\text{c}}, \Phi_{\text{c}}^{\text{L}}, U_{\text{cell}})\, d\zeta, \qquad I_{\text{e}}(t) = \int_{\Omega} i_{\text{e}}(\Phi_{\text{a|c}}^{\text{L}})\, d\zeta, \tag{10}$$

$$i = \left(c_{\text{a}}^{-1} + c_{\text{e}}^{-1} + c_{\text{c}}^{-1}\right)^{-1} \left(\frac{i_{\text{a}} - I_{\text{a}}}{c_{\text{a}}} + \frac{i_{\text{e}} - I_{\text{e}}}{c_{\text{e}}} + \frac{i_{\text{c}} - I_{\text{c}}}{c_{\text{c}}} \right) + I_{\text{cell}}, \tag{11}$$

$$\frac{dw_{\text{m}}}{dt} = \psi_{10}(w_{\text{m}}, \int_{\partial\Omega_{\text{a,out}}} w_{\text{a}}\, d\zeta_2, \int_{\partial\Omega_{\text{a,out}}} \gamma_{\text{a}}\, d\zeta_2, \int_{\partial\Omega_{\text{c,out}}} w_{\text{c}}\, d\zeta_1, \int_{\partial\Omega_{\text{c,out}}} \gamma_{\text{c}}\, d\zeta_1, \lambda_{\text{air}}, \vartheta_{\text{air}}, R_{\text{back}}), \tag{12}$$

$$\gamma_{\text{m}}(t) = \psi_{11}(w_{\text{m}}, \int_{\partial\Omega_{\text{a,out}}} w_{\text{a}}\, d\zeta_2, \int_{\partial\Omega_{\text{a,out}}} \gamma_{\text{a}}\, d\zeta_2, \int_{\partial\Omega_{\text{c,out}}} w_{\text{c}}\, d\zeta_1, \int_{\partial\Omega_{\text{c,out}}} \gamma_{\text{c}}\, d\zeta_1, \lambda_{\text{air}}, \vartheta_{\text{air}}, R_{\text{back}}). \tag{13}$$

3. The initial conditions:

$$\vartheta_{\mathrm{s}}|_{t=0} = \vartheta_{0,\mathrm{s}}(\zeta),\ w_{\mathrm{a}}|_{t=0} = w_{0,\mathrm{a}}(\zeta),\ w_{\mathrm{c}}|_{t=0} = w_{0,\mathrm{c}}(\zeta),\ w_{\mathrm{m}}|_{t=0} = w_{0,\mathrm{m}},$$
$$\Phi_{\mathrm{a}}^{\mathrm{L}}|_{t=0} = \Phi_{0,\mathrm{a}}^{\mathrm{L}}(\zeta),\ \Phi_{\mathrm{c}}^{\mathrm{L}}|_{t=0} = \Phi_{0,\mathrm{c}}^{\mathrm{L}}(\zeta),\ U_{\mathrm{cell}}|_{t=0} = U_{0,\mathrm{cell}}. \tag{14}$$

The PDAE system consists of a parabolic heat equation (1), hyperbolic transport equations (2–3) with fixed wind direction (because $\gamma_{\mathrm{a|c}}, \vartheta_{\mathrm{a|c}}$ are positive), and the partial differential-algebraic equations (4–7). For numerical simulations, the boundary functions $w_{\mathrm{in}}(t)$, $\gamma_{\mathrm{in}}(t)$ at the anode gas inlet and the functions $\lambda_{\mathrm{air}}(t)$, $\vartheta_{\mathrm{air}}(t)$ at the air inlet are prescribed. Some of these quantities, however, will later be used for control purposes; see Chap. 4.

2.2 Index Analysis and MOL Discretization

A detailed index analysis of (1–14) yields the differential time index $\nu_t = 1$ (see [15], some small modifications have to be made in order to handle the cathode recycle, which has been switched off in that paper). Therefore *consistent* initial conditions are given by (14). No initial conditions can be prescribed for the algebraic variables $\gamma_{\mathrm{a|c|m}}, \varphi_{\mathrm{a|c}}, I_{\mathrm{a|c|e}}$.

An obvious numerical approach is the vertical method of lines (MOL) based on a semi-discretization in space. This is alleviated by the a priori knowledge of the wind direction of the hyperbolic equations. A five-point star for the (scaled) Laplacian and suitable conservative upwind formulas are used for the spatial derivatives of the transport equations as well as quadrature formulas for the spatial integrals [14]. This yields a very large (dimension $25N^2+6$, N=spatial discretization) semi-explicit differential-algebraic equation system (DAE) of (perturbation=differential) index $\nu = 1$ of the form

$$M\dot{x}(t) = g(x(t), u(t)), \qquad M[x(0) - x_0] = 0, \qquad M = \mathrm{diag}(I, O)\,. \tag{15}$$

3 Steady State Solution

The numerical procedure to get a steady state solution of (15) for a given constant cell current is intricate, and mimics somehow the starting procedure for a real fuel cell. The difficulties are caused by the unknown initial

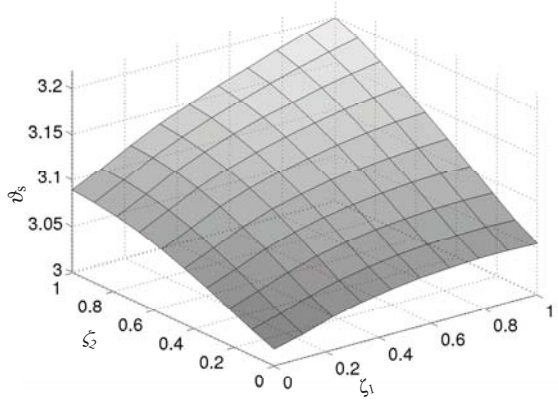

Figure 4: Solid temperature ϑ_{s} (steady state)

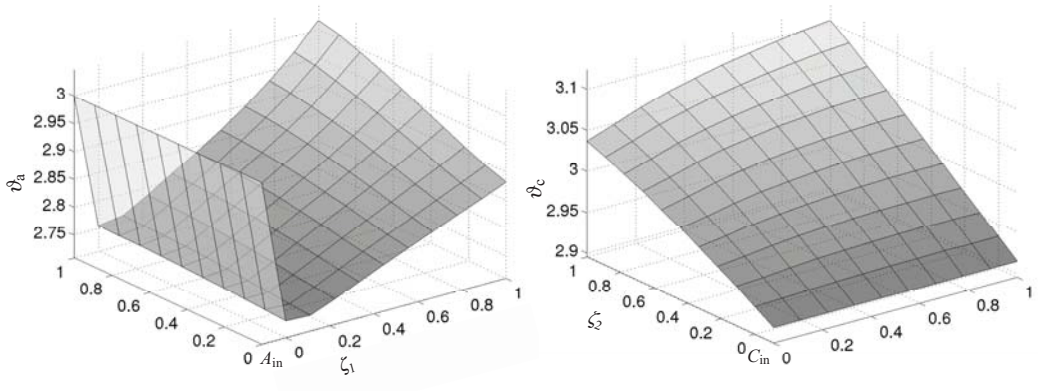

(a) Anode gas temperatur ϑ_{a}

(b) Cathode gas temperature ϑ_{c}

Figure 5: Gas temperatures (steady state)

conditions of the DAE. It consists of a complicated procedure solving firstly only certain equations and then adapting boundary conditions and model constants during the time integration [14]. The computational time to get a steady state solution for a 10×10 discretization is about 1 day on a 1.8 GHz PC. This steady state solution is then stored and used as initial condition for the optimization.

anode gas inlet:	
$\chi_{CH_4,a,in}$	1.0/3.5
$\chi_{H_2O,a,in}$	2.5/3.5
$\vartheta_{a,in}$	3.0
$\gamma_{a,in}$	1.0
air inlet:	
λ_{air}	2.2
ϑ_{air}	1.5
I_{cell}	0.7
R_{back}	0.5

Table 1: Constant boundary data and input data for the steady state solution

The resulting steady state solution is presented in Figs. 4–10 [14], see Table 1 for the used constant boundary data. (Similar steady state solutions have been computed by Heidebrecht [6] using different software packages, here ProMoT [18] and DIVA [12] indicating a correct implementation of the model.)

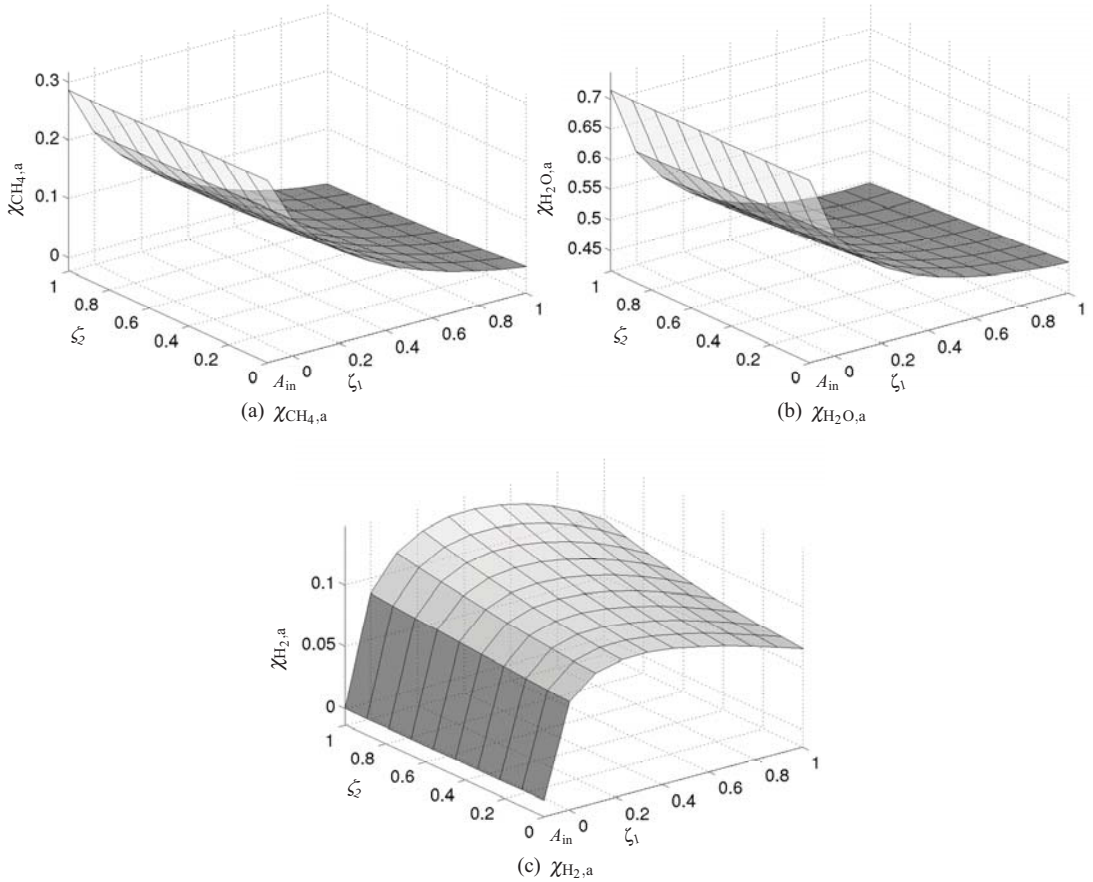

Figure 6: Molar fractions in the anode gas channel (steady state)

The solid temperature ϑ_s is the main quantity of the MCFC model. It describes the temperature distribution of the solid parts, especially in the porous matrix, which is filled by the electrolyte. Figure 4 depicts the steady state solution of ϑ_s; $\vartheta_s = 3.0$ equals 621°C. The solid temperature is dependent on the gas temperatures (Fig. 5) and the exothermic and endothermic reactions. Note that the reaction rates are dependent on the temperature. For example, the solid temperature is extremely high ($\vartheta_s(1,1) = 3.199$ equals 677°C) in the corner ($\zeta_1 = 1, \zeta_2 = 1$), because of the high anode and cathode gas temperatures (see Fig. 5). Analogously, the solid temperature is extremely low ($\vartheta_s(0,0) = 3.017$ equals 627°C) in the corner ($\zeta_1 = 0, \zeta_2 = 0$). Fig. 5 depicts the temperature distribution in the anode and cathode gas channels as well as the boundary data at the gas inlets. The feed gas at the anode inlet is already preheated. At first the anode gas temperature is decreasing in flow direction, because the reforming reactions (ref1,2) are together endothermic. However, the produced hydrogen is used in the exothermic oxidation

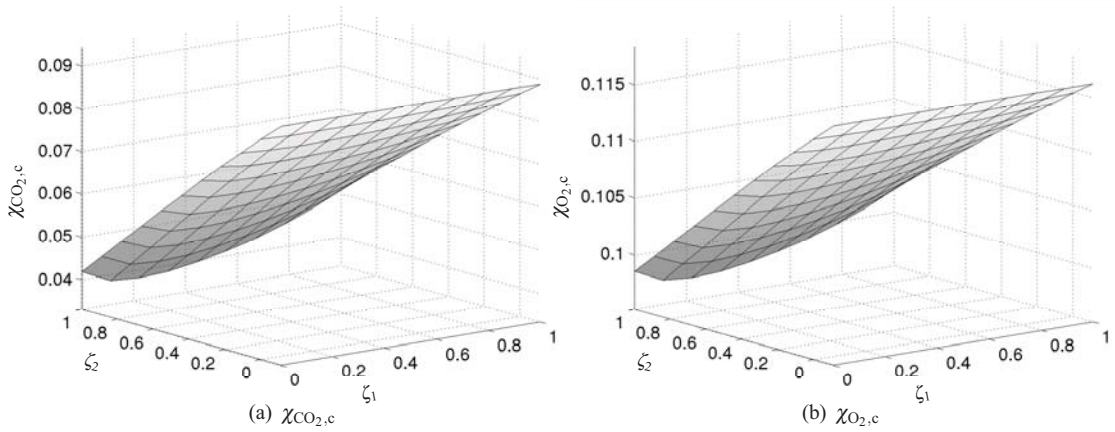

(a) $\chi_{CO_2,c}$ (b) $\chi_{O_2,c}$

Figure 7: Molar fractions in the cathode gas channel (steady state)

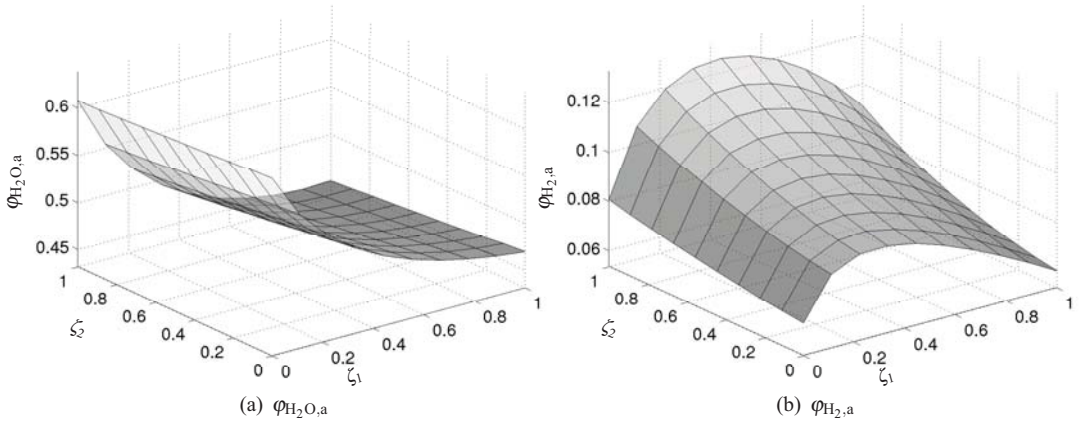

(a) $\varphi_{H_2O,a}$ (b) $\varphi_{H_2,a}$

Figure 8: Partial pressures in anode pores (steady state)

(ox1,2) in the pores. Therefore the anode gas temperature is increasing further downwards. The gas at the anode outlet is further heated in the catalytic burner. In the cathode gas channel, the gas temperature is increasing in flow direction due to the exothermic reduction reaction.

The molar fractions and partial pressures of the gas components are a result of the flow and the five chemical reactions. Figure 6 depicts selected molar fractions in the anode and cathode gas channel, and Figure 8 shows some important partial pressures in the pores of the anode and cathode gas channel. Figure 6(a) shows the decrease of methane, as hydrogen (Fig. 6(c)) is produced. Further down in flow direction, the hydrogen itself decreases again due to the electrochemical oxidation producing finally the electrons. Figure 7 depicts the decrease of oxygen and carbon dioxide in flow direction of the cathode gas channel due to the reduction reaction (red). The produced carbonate ions are transferred from the cathode electrode via the electrolyte to the anode electrode, where they are again used in the oxidation reaction (ox1,2). Methan, hydrogen and carbomonoxideide are negligible in the cathode gas channel, since they have been burnt in the catalytic burner.

Figure 9 presents the molar flow densities and Fig. 10 the electrical potentials Φ_a^L and Φ_c^L. They are correlated with high reaction rates of (ox1,ref) and thus with high solid temperatures (Fig. 4).

The output parameters for the steady state can be found in Table 2; see [9] and [14] for the details.

cell voltage U_{cell}	29.773	0.765 V
cell power P_{cell}	47.638	0.753 kW
electrical efficiency η_{el}	0.497	0.497

Table 2: Output parameter (steady state)

4 Faster Load Changes via Optimal Control

A (possibly discontinuous) change in the input function $I_{\text{cell}}(t)$, typically a piecewise constant function, is called load change. Load changes are technologically important in the production of electrical current. After a load change, the new steady state should be reached as soon as possible, while large gradients of the solid temperature

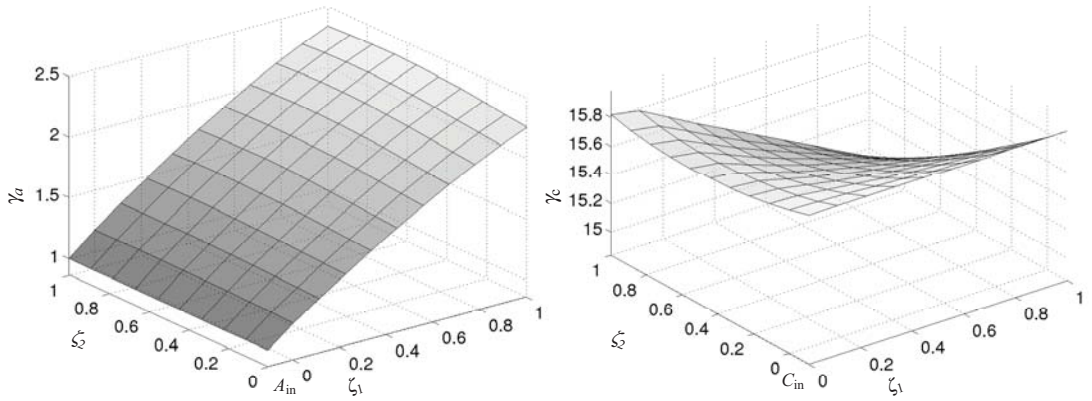

(a) Molar flow density γ_a in anode gas channel (b) Molar flow density γ_c in cathode gas channel

Figure 9: Molar flow density (steady state)

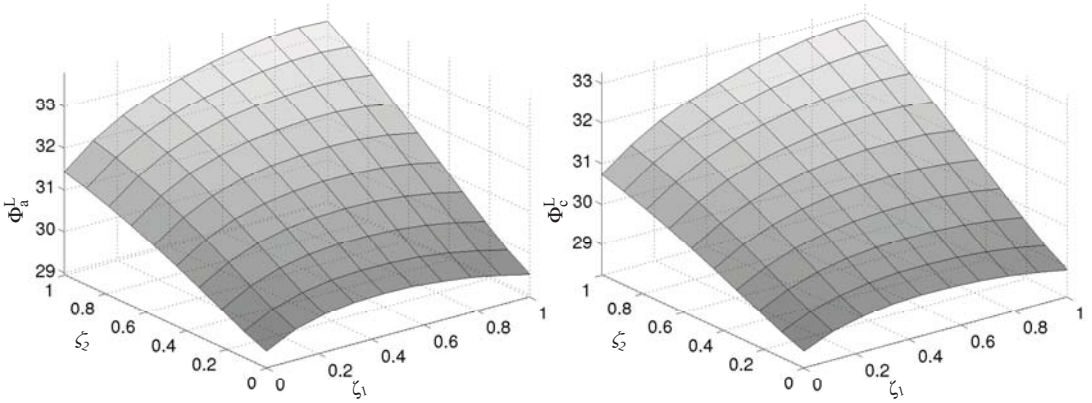

(a) Electrical potential Φ_a^L at anode electrode (b) Electrical potential Φ_c^L at cathode electrode

Figure 10: Electrical potentials (steady state)

have to be avoided. Large temperature gradients yield material stresses and reduce drastically the life-time of the MCFC. The new steady state is reached after approximately $t = 1000$ (3.5 hours), if constant boundary conditions are used in the numerical simulation. A faster approach to the new steady state solution is possible by controlling the boundary conditions at the anode gas inlet and the air inlet via time dependent functions.

As it is technologically possible to control some components of the functions w_{in}, γ_{in}, λ_{air}, ϑ_{air} (they will be denoted by $u(t)$), one can achieve an appropriate trade-off of the two contradicting objectives, i. e. load changes as fast as possible while solid temperature fluctuations stay as small as possible.

Here mathematics can help. Numerical simulations and optimal control of (validated) models based on physical and chemical laws enable forecasts of the behavior of the MCFC without risking the damage of the expensive device. Afterwards it can be decided, if one wants to apply the new control strategies on a real MCFC, or if further model modifications (e.g. further constraints) are necessary.

A load change to higher cell current yields higher material stress. Therefore the following interesting scenario is analyzed:

The input cell current is prescribed as a discontinuous step function

$$I_{\text{cell}}(t) = \begin{cases} I_{\text{cell},1} = 0.7 & \text{if } t \le t^\star, \\ I_{\text{cell},2} = 0.75 & \text{if } t > t^\star. \end{cases} \tag{16}$$

Initial conditions (14) at $t = 0 \le t^\star$ are the steady state solution for constant $I_{\text{cell},1}$.

For the construction of the cost functional, which models the two goals fast load change and small solid temperature gradients in a balanced way, we employ the different time scales of the variables. The solid temperature is the slowest variable. It will deviate at the beginning in the time interval $[t^\star, t_5]$ only slightly from the previous steady state. Therefore it can be neglected in the cost functional during $[t^\star, t_5]$. In $[t^\star, t_5]$ we focus on the fast load change only. Since the cell voltage U_{cell} reacts very fast and significantly on an abrupt load change of the cell current and, in addition, has some impact on the slowest variable (the solid temperature ϑ_{s}), a constant cell voltage is a good *indicator* that the new steady state associated with the new cell current has been reached. In the second time

interval $[t_5, t_f]$ we can then concentrate on small solid temperature differences.

The above approach is especially tailored to handle the Pareto optimal control problem from a practical viewpoint and is modeled as follows:

Find optimal boundary control functions $u : [0, t_f] \to \mathbb{R}^6$, such that the cost functional

$$J[u] = \int_{t^\star}^{t_5} L dt + \int_{t_5}^{t_f} L_5 dt \tag{17}$$

with

$$L = \left[U_{\text{cell}}(t) - U_{\text{cell,2,stat}}\right]^2, \quad U_{\text{cell,2,stat}} = 30.788, \tag{18}$$

$$L_5 = \int_\Omega \left[\vartheta_s(\zeta, t) - \vartheta_{s,\text{ref}}\right]^2 d\zeta, \quad \vartheta_{s,\text{ref}} = 3.1 \tag{19}$$

is minimized s.t. the PDAE/integro-DAE (1–14) and certain control constraints $u(t) \in U$.

In the discretized version, the PDAE/integro-DAE constraint (1–14) is replaced by the semi-explicit DAE (15).

The numerical solution of the large scale DAE-constrained optimal control problem is then computed by the software package NUDOCCCS (Büskens [2]), which transforms this problem into a nonlinear programming problem that is finally solved by an SQP method.

Since the surrogate problem (17, 15) still needs too much computational time, we additionally apply the following modification:

A sequence of optimal control problems

$$\left(\min \int_{t_k}^{t_{k+1}} \tilde{L}_k \, dt \;\text{ s.t. (15) and } u(t) \in U\right)_{k=1,\ldots,5} \tag{20}$$

with $\tilde{L}_k = L$ for $k = 1, 2, 3, 4$, and $\tilde{L}_5 = L_5$ is solved. The bounds of the admissible control set $U \stackrel{\text{def}}{=} \{u \in \mathbb{R}^6 \mid \underline{u}_i \leq u_i \leq \overline{u}_i, i = 1, \ldots, 6\}$ are given in Table 3. The other molar fractions at the anode gas inlet fulfill $\chi_{H_2O,\text{in}} = 1 - \chi_{CH_4,\text{in}}$, $\chi_{k,\text{in}} = 0$, $k \notin \{CH_4, H_2O\}$. A logarithmic-type grid $t_1 = t^\star = 0$, $t_2 = 0.1$, $t_3 = 1.1$, $t_4 = 11.1$, $t_5 = 111.1$,

	$\underline{u}_i$	$u_{i,\text{ref}}$	$\overline{u}_i$
$u_1 = \chi_{CH_4,\text{in}}$	0.25	1.0/3.5	0.35
$u_2 = \gamma_{\text{in}}$	0.9	1.0	1.1
$u_3 = \vartheta_{\text{in}}$	2.9	3.0	3.1
$u_4 = \lambda_{\text{air}}$	1.8	2.2	2.2
$u_5 = \vartheta_{\text{air}}$	1.3	1.5	1.7
$u_6 = R_{\text{back}}$	0.45	0.5	0.55

Table 3: Control constraints and reference values

$t_6 = t_f = 1111.1$ is used according to the different time scales of the variables. Initial conditions for the first optimal control problem are the steady state solution for $I_{\text{cell},1}$. Initial conditions for the k-th optimal control problem are the free final conditions of the $(k-1)$-th optimal control problem.

In each time interval $[t_k, t_{k+1}]$, an equidistant control grid of 21 points is used. Spatial discretization is only 3×3. Nevertheless, the amount of computation time for the last optimal control problem on $[t_5, t_6]$ is 36 hours.

The numerical solution of the solid temperature ϑ_s at t_f in Fig. 11 can be compared with the numerical solution of the optimal control problem (20) with the different cost functional $\tilde{L}_5 = L$ in Fig. 12.

One can clearly see the improved profile of the solid temperature ϑ_s in Fig. 11. The maximum solid temperature is still in the corner $(\zeta_1 = 1, \zeta_2 = 1)$, but the value has changed from 3.217 to 3.120. The coordinates of the minimum solid temperature have changed from the corner $(\zeta_1 = 1, \zeta_2 = 0)$ to the corner $(\zeta_1 = 0, \zeta_2 = 0)$ with its value changing from 3.090 to 3.021. The maximum temperature difference is reduced from 0.196 (58.330°C) to 0.023 (8.760°C).

In order to reach the flat solid temperature distribution of Fig. 11, it is essential to use all six boundary control functions $\chi_{CH_4,\text{in}}$, ϑ_{in}, γ_{in}, λ_{air}, ϑ_{air}, R_{back}. The solid temperature distribution of Fig. 12, which was reached for the six optimal boundary controls with respect to the cost functional $\tilde{L}_5 = L$, can almost be achieved by *only one* control component γ_{in}.

Additional numerical results for other technologically interesting scenarios can be found in [14].

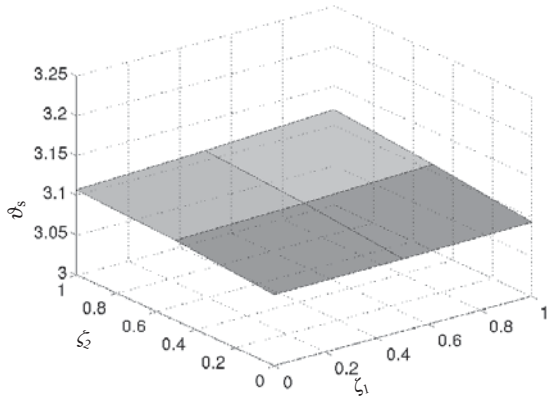

Figure 11: Solid temperatur ϑ_s at time $t_f = 1111.1$ after the load change, with cost functional $\tilde{L}_5 = L_5$ in $[t_5, t_6]$

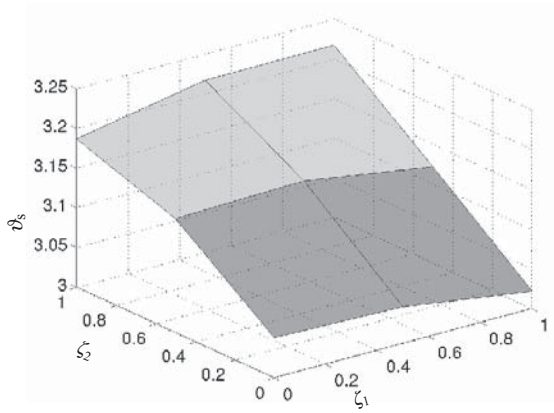

Figure 12: Solid temperatur ϑ_s at $t = 1111.1$ after the load change, with cost functional $\tilde{L}_5 = L$ in $[t_5, t_6]$

5 Conclusions

Numerical simulation and optimal control have been performed for a realistical, detailed, highly complex, large scale mathematical model describing the dynamical behavior of a molten carbonate fuel cell. The validation of a closely related model on a real fuel cell and the very similar results of a numerical simulation by finite volume discretization with respect to both spatial coordinates and solution with ProMoT/DIVA [8] suggest the reliability of the model despite the deficiencies with respect to the resolution of the discretization scheme. Therefore, these simulations and the associated results for the optimally controlled fuel cell (together with the real-time state estimator [4]) will certainly lead to a wider range of admissible operations of MCFC in the future.

A comparison of the numerical results of the 1D counterflow model [3] with the 2D crossflow model yields, that the 2D solid temperature distribution cannot be predicted by the 1D model. However, the numerical results of the different 2D crossflow models suggest that a detailed modeling of the partial pressures of the gas components in the pores can be neglected. Moreover, a combined equation for the two reforming reactions without considering the CO part is also applicable. The resulting deviations are minor; see [14].

Finally, the optimal control results can be further examined by a numerical sensitivity analysis, analogously to the results in [16], but preferably for a simplified model following the above ideas.

Model changes were frequent during the development of the optimal control strategy, but are nowadays seldom. Therefore considerations are now appropriate to use the special structure of the equations and the discretization, especially to use faster linear algebra packages. Moreover the application of model reduction techniques, such as, e.g., proper orthogonal decomposition techniques seems to be inevitable and as the results of [4] show promising, too.

Acknowledgments

We are indebted to Prof. Dr.-Ing. Sundmacher and Dr.-Ing. Heidebrecht from the Max-Planck-Institut für Dynamik komplexer technischer Systeme, Magdeburg, for providing the realistic fuel cell models and to Dr.-Ing.h.c. Berndt and Dipl.-Ing. Koch from the management of the IPF Heizkraftwerksbetriebsges. mbH, Magdeburg, for their continual support. We are indebted to Prof. Dr. Büskens from the University of Bremen for making the direct optimal control software package NUDOCCCS available.

6 References

[1] M. Bischoff, and G. Huppmann, *Operating Experience with a 250 kW_{el} Molten Carbonate Fuel Cell (MCFC) Power Plant,* Journal of Power Sources, **105**, 2 (2002), 216–221.

[2] C. Büskens, *Optimierungsmethoden und Sensitivitätsanalyse für optimale Steuerprozesse mit Steuer- und Zustands-Beschränkungen,* Dissertation, Universität Münster, Germany, 1998.

[3] K. Chudej, M. Bauer, H.J. Pesch, and K. Schittkowski, *Numerical Simulation of a Molten Carbonate Fuel Cell by Partial Differential Algebraic Equations,* in From Nano to Space, Applied Mathematics Inspired by Roland Bulirsch, M. Breitner, G. Denk, P. Rentrop, eds., Springer, Berlin, 2008, 57–70.

[4] M. Grötsch, M. Mangold, M. Sheng, and A. Kienle, *Model Reduction and State Estimation,* in [17], 2007, 185–200.

[5] M. Gundermann, P. Heidebrecht, and K. Sundmacher, *Validation of a Mathematical Model Using an Industrial MCFC Plant,* ASME J. Fuel Cell Sci. Technol. 3 (2006), 303–307.

[6] P. Heidebrecht, *Modelling, Analysis and Optimisation of a Molten Carbonate Fuel Cell with Direct Internal Reforming (DIR-MCFC)*, VDI Fortschritt-Berichte, Reihe 3, Nr. 826, VDI Verlag, Düsseldorf, Germany, 2005.

[7] P. Heidebrecht, and K. Sundmacher, *Optimization of Reforming Catalyst Distribution in a Cross-Flow Molten Carbonate Fuel Cell with Direct Internal Reforming*, Ind. Eng. Chem. Res. 44 (2005), 3522–3528.

[8] P. Heidebrecht, M. Gundermann, and K. Sundmacher, *Steady State and Dynamic Process Analysis*, in [17], 2007, 125–140.

[9] P. Heidebrecht, and K. Sundmacher, *MCFC Reference Model*, in [17], 2007, 35–62.

[10] G. Huppmann, *MTU's Carbonate Fuel Cell HotModule*, in [17], 2007, 3–26.

[11] M. Koch, J. Berndt, and M. Gundermann, *Operational Experiences*, in [17], 2007, 27–32.

[12] R. Köhler, K. Mohl, H. Schramm, M. Zeitz, M. Mangold, E. Stein, and E.D. Gilles, *Method of Lines within the Simulation Enviroment DIVA for Chemical Processes*, in *Adaptive Method of Lines*, A. Vande Wouver, P. Saucez, and W. Schiesser, eds., Chapman & Hall/CRC, Boca Raton, Florida, 2001, 371–406.

[13] S. Rolf, *Betriebserfahrungen mit dem MTU Hot Module,* in Stationäre Brennstoffzellenanlagen, Markteinführung, VDI Berichte, Nr. 1596, VDI Verlag, Düsseldorf, Germany, 2001, 49–57.

[14] K. Sternberg, *Simulation, Optimale Steuerung und Sensitivitätsanalyse einer Schmelzcarbonat--Brennstoffzelle,* Dissertation, Universität Bayreuth, Germany, 2007.

[15] K. Sternberg, K. Chudej, and H.J. Pesch, *Suboptimal control of a 2D molten carbonate fuel cell PDAE model,* Math. Comput. Model. Dyn. Syst. 13, 5 (2007), 471–485.

[16] K. Sternberg, K. Chudej, H.J. Pesch, and A. Rund, *Parametric Sensitivity Analysis of Fast Load Changes of a Dynamic MCFC Model,* ASME J. Fuel Cell Sci. Technol. 5 (2008)

[17] K. Sundmacher, A. Kienle, H.J. Pesch, J.F. Berndt, and G. Huppmann, *Molten Carbonate Fuel Cells – Modeling, Analysis, Simulation, and Control.* Wiley-VCH, Weinheim, Germany, 2007.

[18] T. Tränkle, M. Zeitz, M. Ginkel, and E.D. Gilles *PROMOT: a modeling tool for chemical processes,* Math. Comput. Model. Dyn. Syst. 6, 3 (2000), 283–307.

[19] W. Winkler, *Brennstoffzellenanlagen,* Springer, Berlin, Germany, 2002.